Identification of Novel Inhibitors of the SARS Coronavirus Main Protease 3CL^{pro}†

Usman Bacha,‡ Jennifer Barrila,‡ Adrian Velazquez-Campoy, Stephanie A. Leavitt, and Ernesto Freire*

Department of Biology, Johns Hopkins University, Baltimore, Maryland 21218

Received December 3, 2003; Revised Manuscript Received March 11, 2004

ABSTRACT: SARS (severe acute respiratory syndrome) is caused by a newly discovered coronavirus. A key enzyme for the maturation of this virus and, therefore, a target for drug development is the main protease 3CL^{pro} (also termed SARS-CoV 3CL^{pro}). We have cloned and expressed in *Escherichia coli* the full-length SARS-CoV 3CL^{pro} as well as a truncated form containing only the catalytic domains. The recombinant proteins have been characterized enzymatically using a fluorescently labeled substrate; their structural stability in solution has been determined by differential scanning calorimetry, and novel inhibitors have been discovered. Expression of the catalytic region alone yields a protein with a reduced catalytic efficiency consistent with the proposed regulatory role of the α-helical domain. Differential scanning calorimetry indicates that the α-helical domain does not contribute to the structural stability of the catalytic domains. Analysis of the active site cavity reveals the presence of subsites that can be targeted with specific chemical functionalities. In particular, a cluster of serine residues (Ser139, Ser144, and Ser147) was identified near the active site cavity and was susceptible to being targeted by compounds containing boronic acid. This cluster is highly conserved in similar proteases from other coronaviruses, defining an attractive target for drug development. It was found that bifunctional aryl boronic acid compounds were particularly effective at inhibiting the protease, with inhibition constants as strong as 40 nM. Isothermal titration microcalorimetric experiments indicate that these inhibitors bind reversibly to 3CL^{pro} in an enthalpically favorable fashion, implying that they establish strong interactions with the protease molecule, thus defining attractive molecular scaffolds for further optimization.

From November 2002 through June 2003, more than 8000 persons contracted severe acute respiratory syndrome (SARS), a highly contagious respiratory infection never seen before in humans. The overall mortality rate associated with SARS has been estimated to be close to 10% by the World Health Organization, but exceeded 50% in patients at least 65 years of age. In March 2003, 4 months after the first case was reported, a new coronavirus was identified as the etiological agent of SARS. In April 2003, the complete genome of the virus was sequenced, providing the opportunity for more in-depth studies and the identification of potential targets for drug and vaccine development. The genome sequence of the virus immediately revealed the presence of a protease (3CL^{pro} or SARS-CoV 3CL^{pro}) whose sequence was highly identical to those of proteases known to be essential for the life cycle of other coronaviruses (refs *1*−*3* and unpublished data from this laboratory). In July 2003, one crystallographic structure of 3CL^{pro} was released (PDB entry 1q2w by Bonnano *et al.*). A second structure was published in November 2003 (*4*).

The active site of the SARS-CoV 3CL^{pro} contains a catalytic dyad defined by His41 and Cys145, which is similar to the arrangement found in other coronavirus proteases. From a structural point of view, the catalytic dyad is located in a predominantly β-structure (residues 1−184) reminiscent of the two-domain fold found in the chymotrypsin family (Figure 1). Residues 201−303 form a third compact α-helical domain connected to the catalytic β-domains by a long loop region (residues 185−200). The precise biological role of the α-helical domain is not completely understood, even though it has been hypothesized that it might play a role in

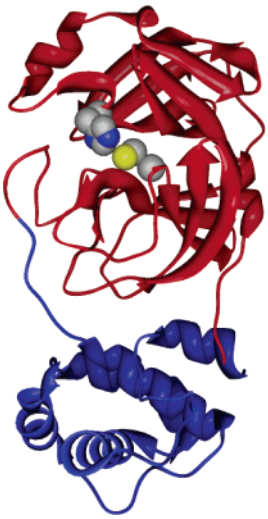

FIGURE 1: Structure of 3CL^{pro} (PDB entry 1q2w) showing the catalytic domains in red and the α-helical domain in blue. Catalytic residues His41 and Cys145 are shown using a van der Waals representation. The color transition (Gln192-Ala193) indicates the point at which a stop codon was placed to express the truncated version of 3CL^{pro}.

† Supported by National Institutes of Health Grant GM 57144.
* To whom correspondence should be addressed.
‡ These authors contributed equally to this paper.

10.1021/bi0361766 CCC: $27.50
Published on Web 03/30/2004

substrate recognition in other coronaviruses (*5*, *6*). From the dimeric structure of SARS-CoV 3CL^{pro}, Yang *et al*. (*4*) have concluded that the helical domain might be responsible for orienting the amino terminus of one monomer to a position in which it can interact with the active site of the other monomer in the dimer. In solution, SARS-CoV 3CL^{pro} is characterized by a weak dimerization constant of 100 μM which is equivalent to 3.4 mg/mL (*7*).

For the studies presented here, we have cloned and expressed in *Escherichia coli* the full length SARS-CoV 3CL^{pro} as well as a truncated form containing only the catalytic domains. The recombinant proteins have been characterized enzymatically using fluorescently labeled substrates; their structural stability in solution has been determined by differential scanning calorimetry, and novel inhibitors have been discovered. Further characterization of these inhibitors suggests that they provide good scaffolds for further optimization and drug development against SARS.

EXPERIMENTAL PROCEDURES

Cloning. cDNA corresponding to the SARS 3CL^{pro} gene (Tor2 strain, GenBank entry AY274119) inserted into a pBR194c vector was kindly provided by the British Columbia Cancer Agency Branch (Vancouver, BC). Competent cells (XL-1 Blue, Stratagene) were transformed for plasmid propagation under ampicillin selection. Plasmid DNA was isolated (Plasmid Midi Kit, Qiagen), and the gene was amplified by PCR with appropriate primers using Pfu Turbo DNA Polymerase (Stratagene). To prevent artifacts, the original plasmid was degraded with a *Dpn*I (Stratagene) digestion reaction (1 h at 37 °C) followed by inactivation of *Dpn*I (20 min at 80 °C). Blunt-end directional cloning was performed by a topoisomerase reaction into a pET100 vector (Champion pET Directional TOPO Expression and Cloning Kit, Invitrogen). The protease gene was cloned in frame with an N-terminal peptide containing a polyhistidine tag for further purification by affinity chromatography. An enterokinase recognition site was present for removal of the amino-terminal tag after purification. As a result, the recombinant protease contains five additional residues (Asp, His, Pro, Phe, and Thr**)** at the amino terminus. One Shot TOP10 competent cells (Invitrogen) were transformed with the product from the cloning reaction. Plasmid DNA was purified, and the gene insertion and its directionality, as well as the integrity of the pET100 vector, were confirmed by DNA sequencing. BL21 Star DE3 (Invitrogen) competent cells were transformed for protein expression under ampicillin selection and IPTG induction.

The gene encoding the truncated protein containing only the catalytic domains was obtained by placing a stop codon in the wild-type plasmid at the position corresponding to Ala193 (Quick Change Site Directed Mutagenesis Kit, Stratagene). After transformation as described above, the plasmid DNA was isolated (Plasmid Midi Kit, Qiagen) and the mutation confirmed by sequencing. BL21 Star DE3 (Invitrogene) competent cells were transformed for protein expression under ampicillin selection and IPTG induction. The truncated protein was expressed and purified in the same manner as wild-type SARS 3CL^{pro}.

Protein Expression and Purification. Plasmid-encoded SARS 3CL^{pro} was expressed as a soluble fraction in BL21 Star DE3 *E. coli* competent cells (Invitrogen). Cells were grown in LB supplemented with ampicillin (50 μg/mL) at 37 °C, induced with IPTG when the optical density was ~0.8, and harvested after 4 h. Cells were resuspended in lysis buffer [50 mM potassium phosphate (pH 7.8), 400 mM sodium chloride, 100 mM potassium chloride, 10% glycerol, 0.5% Triton-X, and 10 mM imidazole] and broken with three passes through a French pressure cell (≥16000 psi). Cell debris was collected by centrifugation (20000*g* at 4 °C for 20 min). The supernatant was filtered using a 0.22 μm pore size filter (Millipore) and applied directly to a nickel affinity column (HisSelect, Sigma) that had been pre-equilibrated with binding buffer [50 mM sodium phosphate, 0.3 M sodium chloride, and 10 mM imidazole (pH 8.0)]. The protease was eluted with a linear gradient of elution buffer [50 mM sodium phosphate, 0.3 M sodium chloride, and 250 mM imidazole (pH 8.0)]. During the concentration of protease fractions, the elution buffer was exchanged gradually with storage buffer [10 mM sodium phosphate, 10 mM sodium chloride, 1 mM TCEP, and 0.5 mM EDTA (pH 7.4)]. The polyhistidine tag of the fusion protein was cut through incubation with 0.1 unit of enterokinase (Invitrogen) per 56 μg of protease for 48 h at 4 °C. The required number of units was determined by setting up pilot reactions using different amounts of enterokinase at different temperatures, and then verifying the efficiency of the reaction by SDS−PAGE. This reaction mixture was passed again through the nickel affinity column, and the flow-through containing the protease was collected. Any residual enterokinase was removed by incubation with EK-away resin (Invitrogen). The sample was diluted 1:4 with storage buffer and concentrated (>10 mg/mL). The purified protein was then stored at −20 °C. The sample was more than 95% pure, as assessed by SDS−PAGE.

Enzymatic Activity. The activity of the full-length and truncated 3CL^{pro} was measured by continuous kinetic assays using the commercially available fluorogenic substrate Dabcyl-Leu-Ala-Gln-Ala-Val-Arg-Ser-Ser-Ser-Arg-Edans (Bachem). The fluorescence intensity was monitored in a Cary Eclipse fluorescence spectrophotometer (Varian) using wavelengths of 330 and 500 nm for excitation and emission, respectively. The experiments were performed with the same buffer used to store the enzyme [10 mM sodium phosphate, 10 mM sodium chloride, 1 mM TCEP, and 0.5 mM EDTA (pH 7.4)]. Kinetic parameters, K_m and k_{cat}, were determined by initial rate measurements at 25 °C. The reaction was initiated by adding protease (final concentration of 1 μM) to a solution containing different final concentrations of the substrate (0−100 μM).

Inhibition Kinetics. FL compounds for inhibition studies were kindly supplied by Fulcrum Pharmaceuticals (Larchmont, NY). Inhibition constants and the inhibition mechanism were assessed by determining the apparent kinetic parameters at (1) a constant substrate concentration and different inhibitor concentrations and (2) constant inhibitor concentrations and variable substrate concentrations. Protease (final concentration of 1 μM) was incubated for 10 min at room temperature with the inhibitor (final concentration of 0−180 μM) and the reaction initiated by adding substrate to the desired final concentration (5 μM for experiments at a constant substrate concentration).

The dependence of the enzymatic rate in terms of substrate and inhibitor concentrations was analyzed in terms of the general equation (see ref *8*)

$$\frac{v_I}{v_0} = \frac{K_m + [S]}{K_m\left(1 + \frac{[I]}{K_i}\right) + [S]\left(1 + \frac{[I]}{\alpha K_i}\right)}$$

where v_I and v_0 are the initial rates at a given inhibitor concentration and without inhibitor, respectively, [S] is the concentration of the substrate, [I] is the concentration of the free inhibitor, K_m is the Michaelis constant, and K_i is the inhibition constant. The parameter α equals ∞ for competitive inhibition, approaches zero for uncompetitive inhibition, and assumes a finite value for noncompetitive inhibition (*8*). All the parameters (K_m, K_i, and α) were determined by global nonlinear regression analysis.

Isothermal Titration Calorimetry. Isothermal titration calorimetry experiments were carried out using a high-precision VP-ITC titration calorimetric system (Microcal Inc.). The enzyme solution in the calorimetric cell was titrated with inhibitor solutions dissolved in the same buffer [10 mM sodium phosphate, 10 mM sodium chloride, 1 mM TCEP, and 0.5 mM EDTA (pH 7.4)]. The heat evolved after each ligand injection was obtained from the integral of the calorimetric signal. The heat due to the binding reaction between the inhibitor and the enzyme was obtained as the difference between the heat of reaction and the corresponding heat of dilution.

Differential Scanning Calorimetry. The heat capacity of full-length and truncated $3CL^{pro}$ was measured as a function of temperature with a high-precision differential scanning VP-DSC microcalorimeter (Microcal Inc., Northampton, MA). Protein samples and reference solutions were properly degassed and carefully loaded into the cells to avoid bubble formation. Thermal denaturation scans were performed with freshly prepared buffer-exchanged protease solutions in 10 mM sodium phosphate, 10 mM sodium chloride, 1 mM TCEP, and 0.5 mM EDTA (pH 7.4). Data were analyzed by software developed in this laboratory.

RESULTS AND DISCUSSION

Enzymatic Activity Measurements. A fluorescence-based enzyme activity assay was implemented to evaluate the inhibitory potency of potential inhibitors. A commercially available fluorogenic peptide (Dabcyl-Leu-Ala-Gln-Ala-Val-Arg-Ser-Ser-Ser-Arg-Edans) that contains the SARS $3CL^{pro}$ Gln-Ala cleavage sequence was used to measure the catalytic rate constants (k_{cat}) and the Michaelis constants (K_m) as described in Experimental Procedures. Figure 2 shows the dependence of the initial enzyme rate on the fluorogenic substrate concentration. The enzyme velocity data are consistent with a K_m of 9 ± 1 μM and a catalytic constant (k_{cat}) of 0.033 ± 0.001 s^{-1} for full-length $3CL^{pro}$ at 25 °C. Incidentally, the N-terminal His-tagged protease exhibited similar enzymatic activity, indicating that the addition of the six histidyl residues to the amino terminus does not significantly affect catalysis. The K_m of the fluorogenic substrate is significantly lower than those reported for unlabeled undecapeptides with sequences corresponding to the cleavage sites in the SARS coronavirus polyprotein (*7*).

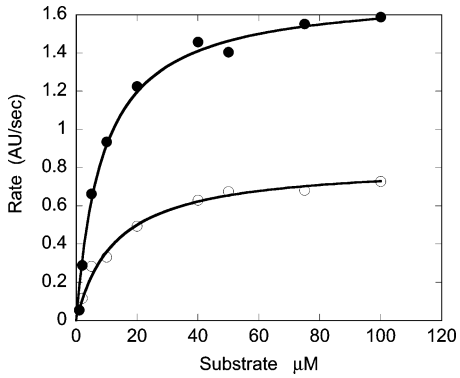

FIGURE 2: Enzymatic activity of full-length (●) and truncated (○) $3CL^{pro}$. The truncated $3CL^{pro}$ contains only the catalytic domains (residues 1−192). Shown in the figure is the initial velocity in arbitrary fluorescence units as a function of substrate concentration. The experiments were performed at 25 °C in 10 mM sodium phosphate, 10 mM sodium chloride, 1 mM TCEP, and 0.5 mM EDTA (pH 7.4).

The fluorogenic substrate contains the correct Gln-Ala cleavage sequence but differs from the viral consensus sequences at positions P4 and P2 [P2, however, has a lower specificity (*4*)]. The lower K_m for the fluorogenic substrate is indicative of a higher affinity for the protease. It is not clear whether the K_m differences are real or the result of different experimental conditions, protein preparations (e.g., N-terminal extension or C-terminal His tag), or assay methods. In fact, similar differences have also been observed for spectroscopic and HPLC-based enzymatic assays of HIV-1 protease substrates (*9*−*21*).

Since the helical domain of $3CL^{pro}$ is supposed to play a role in substrate recognition (*5*, *6*), we decided to investigate the enzyme activity of the isolated catalytic domains. Toward that end, a truncated protein containing only residues 1−192 (shown in red in Figure 1) was also expressed. The catalytic domains alone also exhibited enzymatic activity (Figure 2), albeit with a reduced catalytic efficiency. Its activity is characterized by a K_m of 13 ± 2 μM and a k_{cat} of 0.014 ± 0.001 s^{-1}. The catalytic efficiency of the full-length protease (k_{cat}/K_m) is ~3.5 times higher than that of the truncated protein. Previously, Anand *et al*. (*6*) reported an even larger loss in activity for another coronavirus protease (TGEV $3CL^{pro}$). These differences and the reported preference for substrates with β-sheet-like structures (*7*) suggest that, at a quantitative level, the regulatory role of the helical domain in correctly positioning the substrate for catalysis (*4*−*6*) might depend on the size and structural characteristics of the substrate.

Structural Stability of SARS $3CL^{pro}$. Figure 3 shows the temperature dependence of the heat capacity function of full-length $3CL^{pro}$. The thermal denaturation transition is centered at 52.5 °C under the conditions of these experiments. At pH 7.4, the transition is followed by precipitation, leading to a lack of reversibility in the microcalorimetric scans that precludes a full thermodynamic analysis. Nevertheless, it can be concluded that the transition is highly cooperative and proceeds in a two-state fashion with no indication of independent behavior by either of the domains. Experiments performed at concentrations ranging between 0.17 and 0.4 mg/mL did not exhibit an upward trend in denaturation temperature as could be expected for a dimeric protein. However, these concentrations are well below the dimeriza-

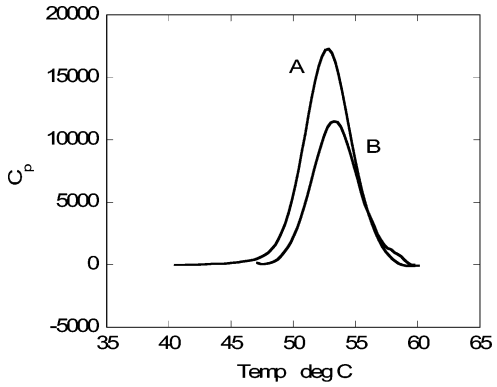

FIGURE 3: Temperature denaturation of full-length (A) and truncated (B) 3CL^{pro} as determined by differential scanning calorimetry. Calorimetric scans for both proteins were performed at identical protein concentrations (0.4 mg/mL) at a scanning rate of 1 °C/min.

tion K_d, and the precipitation observed after denaturation will mask any such dependence. Analytical gel filtration experiments by Fan *et al*. (*7*) indicate that the dimer dissociation midpoint occurs at 3.4 mg/mL. Analytical ultracentrifugation experiments (not shown) are consistent with those results and indicate that at pH 7.4 and protein concentrations of <1.5 mg/mL the protease is mainly monomeric. Microcalorimetric experiments were also performed with the truncated 3CL^{pro} containing only the catalytic domains (Figure 3). The denaturation transition of the truncated 3CL^{pro} is centered at 53.3 °C, a temperature slightly higher than that of full-length 3CL^{pro}, and is also consistent with two-state behavior. In this respect, it has been known for many years that the structurally similar protease chymotrypsin obeys two-state behavior despite being composed of two structural domains similar to those of 3CL^{pro} (*22*). The observation that the truncated protein has a slightly higher stability than the full-length protein is an indication that the α-helical domain is intrinsically less stable and that it derives a significant fraction of its stabilization energy from its interactions with the catalytic domain (see, for example, refs *23* and *24*).

Inhibitor Design. Catalytic residues His41 and Cys145 are located in a relatively shallow cavity between the two domains defining the catalytic site (Figure 4). Close to the catalytic residues is a cluster of serine residues (Ser139, Ser144, and Ser147) that define an attractive subsite for the design of high-affinity inhibitors. Ser144 and Ser147 are located in a cavity that can be targeted by low-molecular weight compounds. The serine cluster is highly conserved in all known coronavirus proteases as illustrated in Figure 5, suggesting that targeting this site might lead to the development of wide-spectrum coronavirus protease inhibitors. In particular, Ser139 and Ser147 are conserved in all known coronaviruses. Ser144 is conserved in 55% of the reported sequences, while in an additional 15% of the sequences, the closely related amino acid threonine occupies that position. The remaining 30% are occupied by alanine. Targeting a highly conserved region among different coronaviruses provides two advantages, the potential for wide-spectrum antivirals and better inhibitor resilience against mutations associated with drug resistance.

Because of the known potential reactivity of boronic acid compounds with the hydroxyl group in serine residues, the

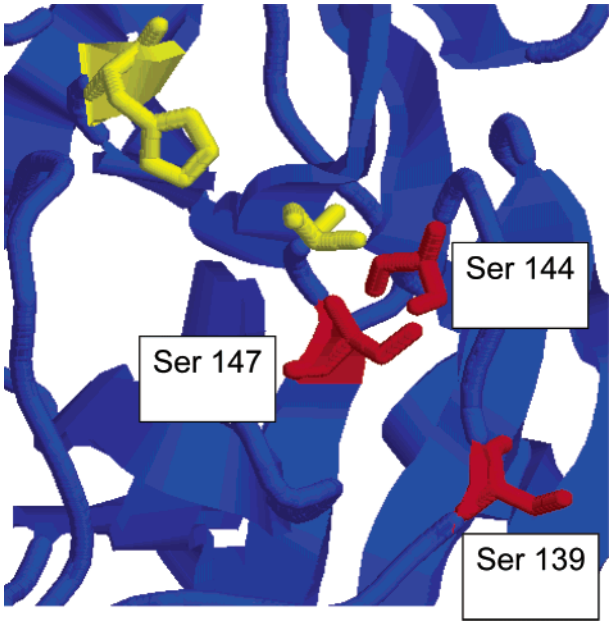

FIGURE 4: Catalytic site of 3CL^{pro} showing the location of Ser139, Ser144, and Ser147 (red). Catalytic residues His41 and Cys145 are shown in yellow. The serine cluster defines an attractive subsite for targeting by potential inhibitors.

inhibitory potency of bifunctional boronic acid compounds was evaluated. A chemical scaffold containing two phenyl boronic groups (FL-078, chemical structure given in Table 1) attached to a central aromatic ring by ester linkages was tested. The compound was shown to have inhibitory activity. Figure 6A shows the dependence of enzyme activity on the concentration of compound FL-078. The inhibitor is characterized by an inhibition constant in the low micromolar range ($K_i = 4.5\ \mu$M). To elucidate the inhibition mechanism of this chemical scaffold, inhibition kinetic experiments were performed at different constant inhibitor concentrations. The results are shown in Figure 6B and indicate that the inhibitor affects not only the apparent K_m but also the V_{max}. This behavior is consistent with a molecule that binds to both the free enzyme and the enzyme−substrate complex. The reversibility of the inhibition mechanism was examined by incubating the enzyme with excess inhibitor (200 μM) and then diluting the inhibitor concentration immediately before the enzyme activity assay. The kinetic parameters were the same in both cases. Accordingly, the data were analyzed by global nonlinear least-squares analysis with the general equilibrium model discussed by Copeland (*8*) and the equations described in Experimental Procedures. Different variations of FL-078 were tested, including several isomers, replacement of the central aromatic ring with shorter linkers, different functionalities at the linker region, and different functionalities at the phenyl boronic rings. The highest improvement in affinity was observed when the ester linkage between aromatic rings was replaced with an amide group, resulting in nanomolar binding affinities. Table 1 summarizes the inhibition constants (K_i) for five representative compounds. Besides the inhibition constants, of particular interest is the parameter α, which ranges between 1.5 and 5.6 for the inhibitors included in Table 1. For a purely competitive inhibitor, $\alpha = \infty$, whereas for a noncompetitive inhibitor, α ranges somewhere between 1 and ∞. If $\alpha = 1$, the inhibitor binds with equal affinity to the free enzyme and to the

```
                                  ....|....| ....|....| ....|....| ....|....|
                                          130        140        150        160
SARS-CoV              GSPSGVYQCA MRPNHTIKGS FLNGSCGSVG FNIDYDCVSF
MHV ML-10             GRPQGAFHVT LRSSHTIKGS FLCGSCGSVG YVLTGDSVRF
MHV A59               GRPQGAFHVT LRSSHTIKGS FLCGSCGSVG YVLTGDSVRF
MHV JHM               GRPQGAFHVV MRSSHTIKGS FLCGSCGSVG YVLTGDSVRF
MHV-2                 GKSQGAFHVT MRSSYTIKGS FLCGSCGSVG YVLTGDSVRF
MHV Penn 97-1         GKSQGAFHVT MRSSYTIKGS FLCGSCGSVG YVLTGDSVRF
MHV ML-11             GKSQGAFHVT MRSSYTIKGS FLCGSCGSVG YVLTGDSVRF
BCV Quebec            GKPQGAFHVT MRSSYTIKGS FLCGSCGSVG YVIMGDCVKF
BCV LUN               GKPQGAFHVT MRSSYTIKGS FLCGSCGSVG YVLMGDCVKF
BCV Mebus             GKPQGAFHVT MRSSYTIKGS FLCGSCGSVV YVIMGDCVKF
BCV ENT               GKPQGAFHVT MRSSYTIKGS FLCGSCGSVG YVLMGDCVKF
PEDV-CV777            GAAAGVYGVN MRSNYTIRGS FINGACGSPG YNINNGTVEF
TGEV Purdue-115       GCPGSVYGVN MRSQGTIKGS FIAGTCGSVG YVLENGILYF
TGEV PUR46-MAD        GCPGSVYGVN MRSQGTIKGS FIAGTCGSVG YVLENGILYF
FIPV 79-1146          GCPGSVYGVN MRSQGTIKGS FIAGTCGSVG YVLENGTLYF
HCV 229E              GCAQGVFGVN MRTNWTIRGS FINGACGSPG YNLKNGEVEF
IBV Beaudette         GTVVGLYPVT MRSNGTIRAS FLAGACGSVG FNIEKGVVNF
IBV LX4               GTVIGLYPVT MRSNGTIRAS FLAGACGSVG FNIERGVVNF
IBV Beaudette CK      GTVVGLYPVT MRSNGTIRAS FLAGACGSVG FNIEKGVVNF
IBV BJ                GTVIGLYPVT MRSNGTIRAS FLAGACGSVG FNIEKGVVNF
                                             139       144   147
```

FIGURE 5: Sequence alignment of the region containing the serine cluster (Ser139, Ser144, and Ser147) among proteases from different coronaviruses. GenBank accession numbers for protein sequences follow: NP_828863 for SARS-HCV (severe acute respiratory syndrome human coronavirus), AAF69341 for MHV ML-10 (murine hepatitis virus strain ML-10), NP_740610 for MHV A59 (murine hepatitis virus strain A59), P19751 for MHV JHM (murine hepatitis virus strain JHM), AAF19383 for MHV-2 (murine hepatitis virus strain 2), AAF69331 for MHV Penn 97-1 (murine hepatitis virus strain Penn 97-1), AAF68919 for MHV ML-11 (murine hepatitis virus strain ML-11), AAL40396 for BCV Quebec (bovine coronavirus strain Quebec), AAL57315 for BCV LUN (bovine coronavirus strain LUN), AAA64744 for BCV Mebus (bovine coronavirus strain Mebus), NP_742132 for BCV ENT (bovine coronavirus strain ENT), NP_839959 for PEDV-CV777 (porcine epidemic diarrhea virus strain CV777), CAA83979 for TGEV Purdue-115 (transmissible gastroenteritis virus strain Purdue-115), NP_840003 for TGEV PUR46-MAD (transmissible gastroenteritis virus strain PUR46-MAD), AAK09095 for FIPV 79-1146 (feline infectious peritonitis virus strain 79-1146), NP_835346 for HCV 229E (human coronavirus strain 229E), NP_740623 for IBV Beaudette (avian infectious bronchitis virus strain Beaudette), AAQ21584 for IBV LX4 (avian infectious bronchitis virus strain LX4), CAC39112 for IBV Beaudette CK (avian infectious bronchitis virus strain Beaudette CK), and AAP92674 for IBV BJ (avian infectious bronchitis virus strain BJ).

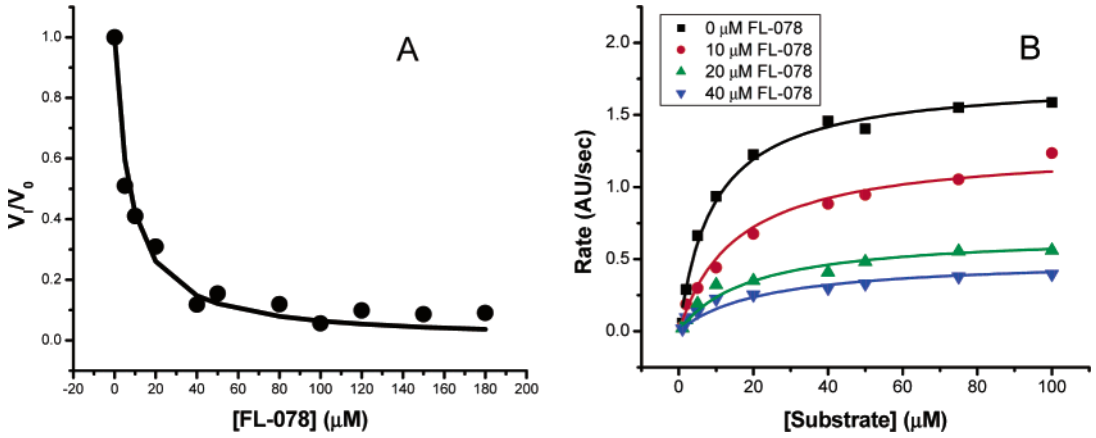

FIGURE 6: Inhibition of SARS-associated $3CL^{pro}$ by compound FL-078 (see Table 1). Shown in panel A is the decrease in enzyme activity as a function of inhibitor concentration at 5 μM S. Shown in panel B is the dependence of enzyme activity on substrate concentration at different constant inhibitor concentrations. Analysis of the data indicates that the inhibitors considered here are noncompetitive and affect both K_m and V_{max} (see the text for details). Solid lines correspond to a best parameter fit (Table 1).

enzyme–substrate complex. For the inhibitors in Table 1, the affinity is higher for the free enzyme by factors ranging between 1.5 and 5.6, but significant affinity for the enzyme–substrate complex is maintained. This is somewhat expected from the structural location of the targeted serine cluster in relation to the catalytic dyad. It can be suggested, however, that inhibition of substrates larger than the decapeptide substrate used in these studies might exhibit a more competitive nature if they require a larger binding footprint and their binding is additionally compromised by the presence of the inhibitor. Analysis of the inhibition data in terms of Dixon plots (not shown) yielded a linear dependence of $1/v$ on inhibitor concentration ($r^2 = 0.97$), indicating that the enzyme–substrate–inhibitor complex is not catalytically active; i.e., the parameter β is equal to zero according to standard nomenclature (*8*, *25*). The truncated form of the enzyme was equally inhibited by the bifunctional aryl boronic acid compounds studied here, consistent with the idea that these compounds target the catalytic and not the α-helical domain.

Isothermal titration calorimetric experiments (Table 1) indicate that the inhibitors studied here bind to $3CL^{pro}$ with

Table 1: 3CL^{pro} Inhibition Parameters for Bifunctional Aryl Boronic Compounds

Name	Structure	MW	K_i μM	α	ΔH kcal/mol	-TΔS kcal/mol
FL-078	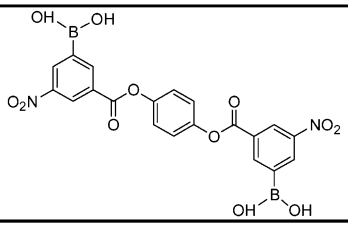	496	4.5	3.3	-5 ± 1	-2
FL-101	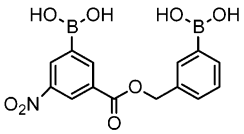	344	16	4.2	-2 ± 1	-5
FL-106	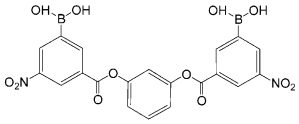	496	6.0	5.6	-4 ± 2	-3
FL-136	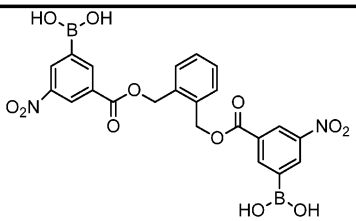	524	6	2.5	-5 ± 2	-2
FL-166	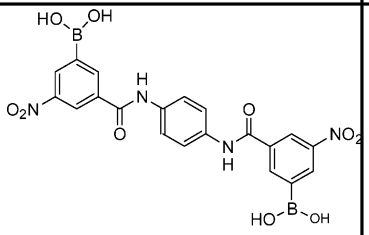	494	0.04	1.8	-5 ± 2	-5

favorable enthalpic and entropic contributions. This thermodynamic profile is characteristic of a binding process driven by favorable inhibitor−protein interactions and not only by water exclusion due to hydrophobicity (*26*−*28*). It has been argued that enthalpically favorable lead compounds must be preferred over entropically driven ones since further optimization can be more readily accomplished (*26*−*28*).

The compounds studied here have molecular weights ranging between 344 and 524 and are characterized by inhibition constants as low as the midnanomolar range; as such, they provide attractive scaffolds for drug design. Currently, we are engaged in the optimization of these scaffolds as potential anti-SARS drugs. The results will be the topic of a future communication.

ACKNOWLEDGMENT

To the British Columbia Cancer Agency Branch for providing the SARS 3CL^{pro} protease gene, to Fulcrum Pharmaceuticals for providing the bifunctional aryl boronic acid compounds, and to Professor Evangelous Moudrianakis for performing the analytical ultracentrifugation experiments. Figure 1 was produced using the UCSF Chimera package from the Computer Graphics Laboratory, University of California, San Francisco (supported by Grant NIH P41 RR-01081).

REFERENCES

1. Anand, K., Ziebuhr, J., Wadhwani, P., Mesters, J. R., and Hilgenfeld, R. (2003) Coronavirus main proteinase (3CL^{pro}) Structure: Basis for design of Anti-SARS Drugs, *Science 300*, 1763−1767.
2. Kim, J. C., Spence, R. A., Currier, P. F., Lu, X., and Denison, M. R. (1995) Coronavirus protein processing and RNA synthesis is inhibited by the cysteine proteinase inhibitor E64d, *Virology 208*, 1−8.
3. Ziebuhr, J., Heusipp, G., and Siddell, S. G. (1997) Biosynthesis, purification and characterization of the human coronavirus 229E 3C-like proteinase, *J. Virol. 71*, 3992−3997.
4. Yang, H., Yang, M., Ding, Y., Liu, Y., Lou, Z., Zhou, Z., Sun, L., Mo, L., Ye, S., Pang, H., Gao, G. F., Anand, K., Bartlam, M., Hilgenfeld, R., and Rao, Z. (2003) The crystal structures of severe acute respiratory syndrome virus main protease and its complex with an inhibitor, *Proc. Natl. Acad. Sci. U.S.A. 100*, 13190−13195.
5. Ziebuhr, J., Snijder, E. J., and Gorbalenya, A. (2000) Virus-encoded proteinases and proteolytic processing in the Nidovirales, *J. Gen. Virol. 81*, 853−879.
6. Anand, K., Palm, G. J., Mesters, J. R., Siddell, S. G., Ziebuhr, J., and Hilgenfeld, R. (2002) Structure of coronavirus main proteinase

reveals combination of a chymotrypsin fold with an extra α-helical domain, *EMBO J. 21*, 3213−3224.

7. Fan, K., Wei, P., Feng, Q., Chen, S., Huang, C., Ma, L., Lai, B., Pei, J., Liu, Y., Chen, J., and Lai, L. (2004) Biosynthesis, purification, and substrate specificity of severe acute respiratory syndrome coronavirus 3C-like proteinase, *J. Biol. Chem. 279*, 1637−1642.
8. Copeland, R. A. (2000) *Enzymes: A practical introduction to structure, mechanism and data analysis*, 2nd ed., Wiley-VCH, New York.
9. Muzammil, S., Ross, P., and Freire, E. (2003) A major role for a set of non-active site mutations in the development of HIV-1 protease drug resistance, *Biochemistry 42*, 631−638.
10. Nillroth, U., Vrang, L., Markgren, P. O., Hulten, J., Hallberg, A., and Danielson, U. H. (1997) Human immunodeficiency virus type 1 proteinase resistance to symmetric cyclic urea inhibitor analogs, *Antimicrob. Agents Chemother. 41*, 2383−2388.
11. Velazquez-Campoy, A., Todd, M. J., Vega, S., and Freire, E. (2001) Catalytic Efficiency and Vitality of HIV-1 Proteases from African Viral Subtypes, *Proc. Natl. Acad. Sci. U.S.A. 98*, 6062−6067.
12. Maschera, B., Darby, G., Palu, G., Wright, L. L., Tisdale, M., Meyers, R., Blair, E. D., and Furfine, E. S. (1996) Human immunodeficiency virus. Mutations in the viral protease that confers resistance to saquinavir increase the dissociation rate constant of the protease-saquinavir complex, *J. Biol. Chem. 271*, 33231−33235.
13. Ermolieff, J., Lin, X. L., and Tang, J. (1997) Kinetic properties of saquinavir-resistant mutants of human immunodeficiency virus type 1 protease and their implications in drug resistance in vivo, *Biochemistry 36*, 12364−12370.
14. Pazhanisamy, S., Stuver, C. M., Cullinan, A. B., Margolin, N., Rao, B. G., and Livingston, D. J. (1996) Kinetic Characterization of Human Immunodeficiency Virus Type-1 Protease-resistant Variants, *J. Biol. Chem. 271*, 17979−17985.
15. Feher, A., Weber, I. T., Bagossi, P., Boross, P., Mahalingam, B., Louis, J. M., Copeland, T. D., Torshin, I. Y., Harrison, R. W., and Tozzer, J. (2002) Effect of sequence polymorphism and drug resistance on two HIV-1 Gag processing sites, *Eur. J. Biochem. 269*, 4114−4120.
16. Patick, A. K., Rose, R., Greytok, J., Bechtold, C. M., Hermsmeier, M. A., Chen, P. T., Barrish, J. C., Zahler, R., Colonno, R. J., and Lin, P. F. (1995) Characterization of a Human-Immunodeficiency-Virus Type-1 Variant with Reduced Sensitivity to an Aminodiol Protease Inhibitor, *J. Virol. 69*, 2148−2152.
17. Schock, H. B., Garsky, V. M., and Kuo, L. C. (1996) Mutational anatomy of an HIV-1 protease variant conferring cross-resistance to protease inhibitors in clinical trials: Compensatory modulations of binding and activity, *J. Biol. Chem. 271*, 31957−31963.
18. Ridky, T. W., Kikonyogo, A., and Leis, J. (1998) Drug-resistant HIV-1 proteases identify enzyme residues important for substrate selection and catalytic rate, *Biochemistry 37*, 13835−13845.
19. Gulnik, S. V., Suvorov, L. I., Liu, B. S., Yu, B., Anderson, B., Mitsuya, H., and Erickson, J. W. (1995) Kinetic Characterization and Cross-Resistance Patterns of Hiv-1 Protease Mutants Selected under Drug Pressure, *Biochemistry 34*, 9282−9287.
20. Mahalingam, B., Boross, P., Wang, Y. F., Louis, J. M., Fischer, C. C., Tozser, J., Harrison, R. W., and Weber, I. T. (2002) Combining mutations in HIV-1 protease to understand mechanisms of resistance, *Proteins 48*, 107−116.
21. Shao, W., Everitt, L., Manchester, M., Loeb, D. D., Hutchison, C. A., and Swanstrom, R. (1997) Sequence requirements of the HIV-1 protease flap region determined by saturation mutagenesis and kinetic analysis of flap mutants, *Proc. Natl. Acad. Sci. U.S.A. 94*, 2243−2248.
22. Privalov, P. L., and Khechinashvili, N. N. (1974) A Thermodynamic Approach to the Problem of Stabilization of Globular Protein Structure: A Calorimetric Study, *J. Mol. Biol. 86*, 665−684.
23. Licalsi, C., Freire, E., and Roseman, S. (1991) Sugar Transport by the Bacterial Phosphotransferase System: Structural and Thermodynamic Domains of Enzyme I of *Salmonella typhimurium*, *J. Biol. Chem. 266*, 19519−19527.
24. Luque, I., Leavitt, S. A., and Freire, E. (2002) The linkage between protein folding and functional cooperativity: two sides of the same coin? *Annu. Rev. Biophys. Biomol. Struct. 31*, 235−256.
25. Alur, H. H., Desai, R. P., Mitra, A. K., and Johnston, T. P. (2001) Inhibition of a model protease: pyroglutamate aminopeptidase by natural oligosaccharide gum from *Hakea gibbosa*, *Int. J. Pharm. 212*, 171−176.
26. Ohtaka, H., Velazquez-Campoy, A., Xie, D., and Freire, E. (2002) Overcoming Drug Resistance in HIV-1 Chemotherapy: The Binding Thermodynamics of Amprenavir and TMC-126 to Wild-Type and Drug-Resistant Mutants of the HIV-1 Protease, *Protein Sci. 11*, 1908−1916.
27. Velazquez-Campoy, A., Todd, M. J., and Freire, E. (2000) HIV-1 Protease Inhibitors: Enthalpic versus Entropic Optimization of the Binding Affinity, *Biochemistry 39*, 2201−2207.
28. Velazquez-Campoy, A., Luque, I., Todd, M. J., Milutinovich, M., Kiso, Y., and Freire, E. (2000) Thermodynamic Dissection of the Binding Energetics of KNI-272, a Powerful HIV-1 Protease Inhibitor, *Protein Sci. 9*, 1801−1809.

BI0361766